ACS OMEGA

http://pubs.acs.org/journal/acsodf

Article

In Situ Small-Angle X-ray Scattering Studies on the Growth Mechanism of Anisotropic Platinum Nanoparticles

Wataru Yoshimune,* Akira Kuwaki,* Takumi Kusano, Takuro Matsunaga, and Hiroshi Nakamura

Cite This: *ACS Omega* 2021, 6, 10866−10874

Read Online

ACCESS | Metrics & More | Article Recommendations | Supporting Information

ABSTRACT: Shape-controlled platinum nanoparticles exhibit extremely high oxygen reduction activity. Platinum nanoparticles were synthesized by the reduction of a platinum complex in the presence of a soft template formed by organic surfactants in oleylamine. The formation of platinum nanoparticles was investigated using in situ small-angle X-ray scattering experiments. Time-resolved measurements revealed that different particle shapes appeared during the reaction. After the nuclei were generated, they grew into anisotropic rod-shaped nanoparticles. The shape, size, number density, reaction yield, and specific surface area of the nanoparticles were successfully determined using small-angle X-ray scattering profiles. Anisotropic platinum nanoparticles appeared at a low reaction temperature (∼100 °C) after a short reaction time (∼30 min). The aspect ratio of these platinum nanoparticles was correlated with the local packing motifs of the surfactant molecules and their stability. Our findings suggest that the interfacial structure between the surfactant and platinum nuclei can be important as a controlling factor for tailoring the aspect ratio of platinum nanoparticles and further optimizing the fuel cell performance.

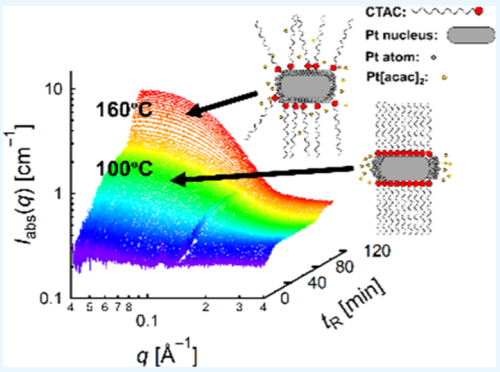

■ INTRODUCTION

Metal nanoparticles (NPs) have attracted attention because of their unique physicochemical properties such as local surface plasmon phenomena,[1,2] spin polarization,[3,4] and catalytic activity,[5,6] which differ from their bulk properties. Shape control is effective in the design of these physicochemical properties.[7] Recently, shape-controlled platinum and platinum-based NPs have been studied for their mass activity in the oxygen reduction reaction.[8−15] Anisotropic shapes have excellent electron conductivity, an electrochemically active surface area (ECSA), and specific activity. It is worth noting that Arenz et al. presented a breakthrough concept for a self-supported Pt−CoO catalyst capable of combining high specific activity with an unprecedentedly high ECSA.[16] However, it is still essential to control the shape of platinum NPs for fuel cell applications.

The growth mechanism of anisotropic gold NPs has been rigorously investigated for electronics and biomedical applications[17,18] because anisotropic gold NPs have two types of localized surface plasmon absorption bands corresponding to the short and long axes of elliptical NPs. These absorption bands vary along short and long axis lengths. In the above-mentioned fields, precise control of the aspect ratio has a critical effect on these properties. Therefore, various synthesis methods have been proposed to design the shape of gold NPs: electrochemical methods,[19] photochemical reaction methods,[20] and seed-mediated colloid growth methods.[21] In the seed-mediated colloid growth method, anisotropic gold NPs are grown using a surfactant as a soft template. The surfactant selectively adsorbed onto the metal surface promoted the anisotropic growth of the nucleus.

As Quinson and Jensen summarized in their review article,[22] a variety of approaches have been reported to obtain platinum NPs. Similarly, a review focused on their shape control was summarized by Cheong et al.[23] For fuel cell applications, the seed-mediated colloid growth method has often been applied to the synthesis of anisotropic platinum NPs. Note that research is being conducted on surfactant-free synthesis[23] or the surfactant removal process[24] since the process of removing surfactants is necessary.[25] An extreme heating treatment (>100 °C) for several hours was found to be an effective synthetic protocol for the seed-mediated colloid growth method of platinum NPs.[14,15,26,27] Their reaction conditions are different from those of gold NP synthesis (typically a milli-second-scale reaction at around room temperature). This is likely due to their ionization properties. The nuclei of metal NPs must be reduced from a metal cation M(X) to a metal M(0) in the liquid phase, where the metal salt is dissolved. The most reducible Au(III) ion enables the growth of gold NPs under mild reaction conditions in a few seconds.[17,21] Polte et al.

Received: February 2, 2021
Accepted: April 1, 2021
Published: April 13, 2021

ACS Publications

© 2021 The Authors. Published by American Chemical Society

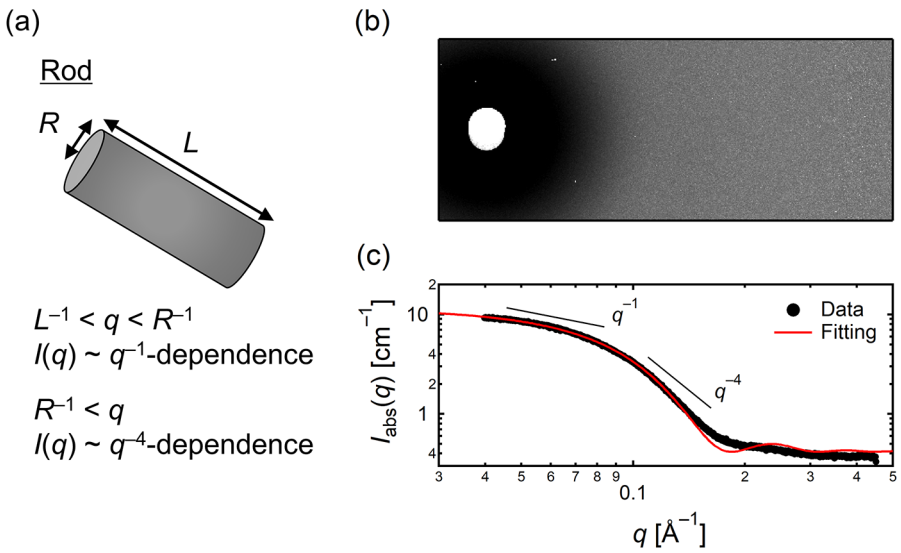

Figure 1. (a) Illustration of a rod with radius R [Å] and length L [Å] oriented in the direction of angle α [rad] for the referential axis. (b) 2D SAXS patterns of platinum NPs synthesized by heating at 160 °C for 100 min. (c) Circular averaged 1D SAXS profiles.

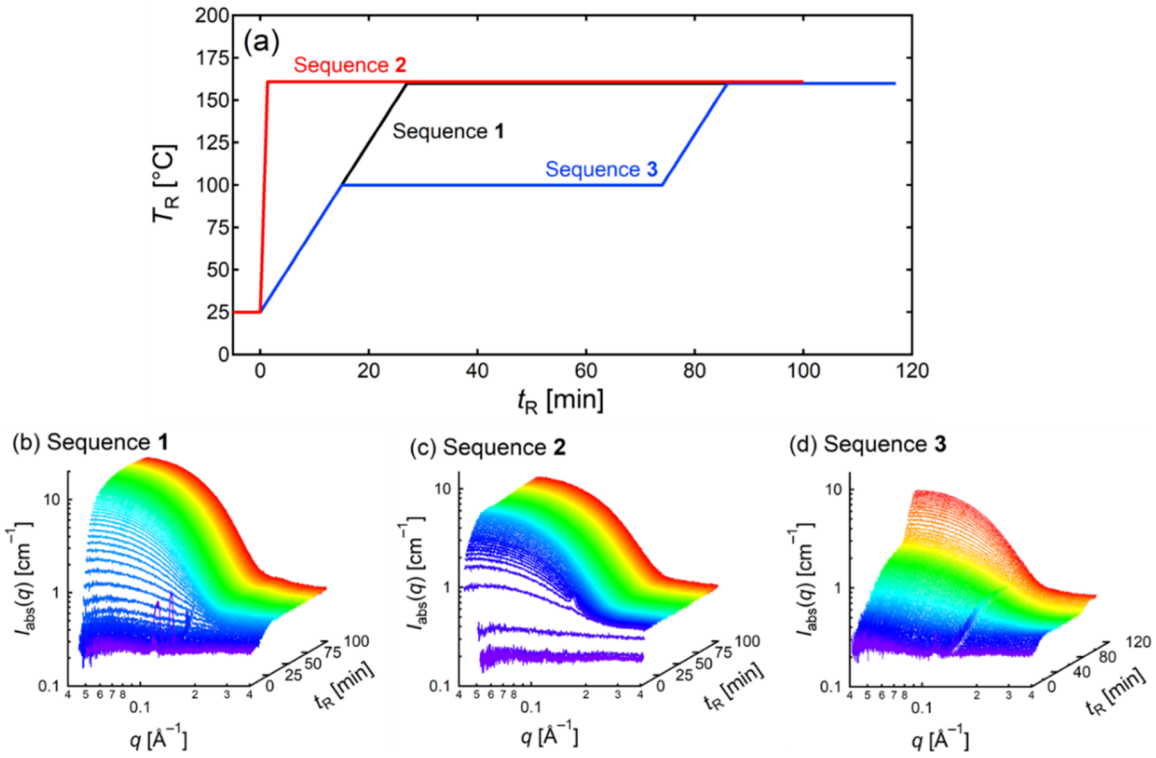

Figure 2. (a) Heating sequences for the in situ time-resolved SAXS study. T_R and t_R represent reaction temperature and reaction time, respectively. In sequences **1** and **3**, the heating rate was fixed at 5 °C/min. In sequence **2**, the heating rate was fixed at 100 °C/min. T_R was held at 160 °C in sequences **1** and **2**. In sequence **3**, T_R was held at 100 °C for 60 min and finally increased to 160 °C. (b−d) In situ SAXS profiles as a function of reaction time t_R in sequences **1**−**3**.

investigated the differences and similarities between the formation processes of gold and silver NPs.[28] They claimed that the growth mechanism of gold NPs consists of only one process of coalescence that proceeds within a few seconds after mixing the reactants, while the growth of silver NPs proceeds via two distinct coalescence processes. For this reason, it is difficult to find studies on the formation mechanism of gold NPs under high-temperature conditions. However, in situ studies on the formation process of platinum NPs under high-temperature reactions have been reported elsewhere.[29−37] The reaction temperature and pressure strongly influence the structure, size, and shape of the NPs.[36,37] However, to the best of our knowledge, the effect of synthetic protocols on the seed-mediated colloid growth method of platinum NPs, such as heating temperature, time, and rate, on the shape, size, number density, reaction yield, and specific surface area (SSA) of platinum NPs has not yet been investigated for fuel cell applications.

https://doi.org/10.1021/acsomega.1c00608
ACS Omega 2021, 6, 10866−10874

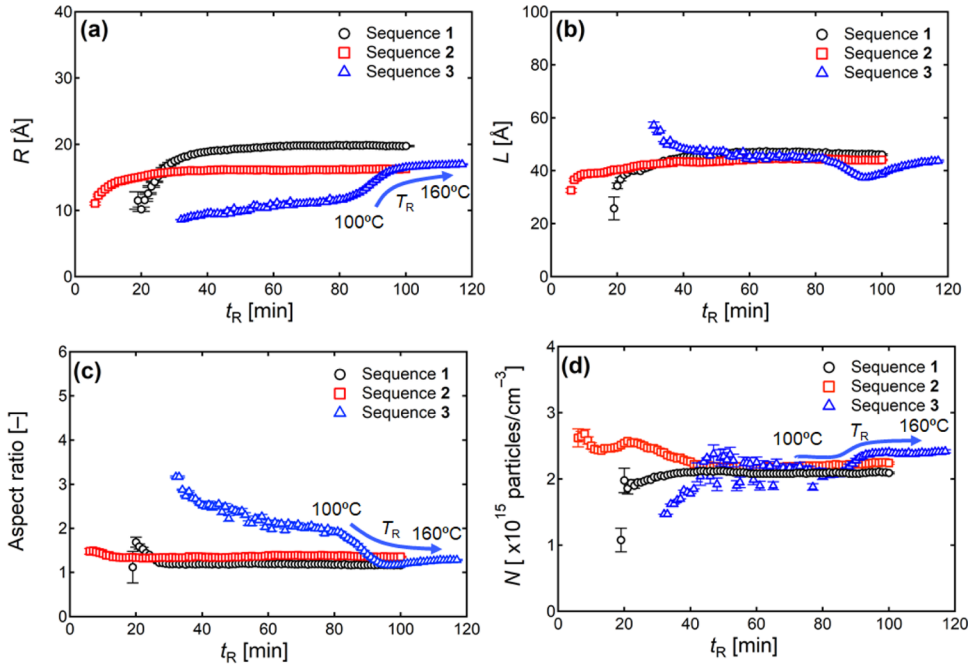

Figure 3. Structural evolution as a function of reaction time t_R for anisotropic platinum NPs: (a) rod radius R [Å], (b) rod length L [Å], (c) aspect ratio [—] equal to $L/2R$, and (d) number density of particles N [particles cm^{-3}]. Immediately after the start of the reaction, the obtained fitting parameters were scattered because the weak signals shown in Figure 2 were not properly fitted by the rod model.

Real-time transmission electron microscopy (TEM) observation[38] during the synthesis of metal NPs provides direct evidence of the formation process of metal NPs, but this cutting-edge technology is not suitable for platinum NPs because it requires a high-temperature reaction. In such cases, it is useful to perform X-ray absorption fine structure (XAFS) and small-angle X-ray scattering (SAXS) measurements.[39] From the results of in situ quick XAFS measurements, the stages of the reduction−nucleation, aggregative particle growth, and Ostwald ripening of metal atoms to produce metal NPs were discriminated in course of reduction time.[39−42] Additionally, SAXS measurements allow for the quantitative analysis of growth progress using parameters such as shape, size, and number density of metal NPs.[39] Since the mid-2000s, in situ time-resolved SAXS measurements have been established to study the formation process of gold NPs, leading to a deeper understanding of the growth mechanism.[43] Currently, this technique is widely applied to monitor the nucleation and formation processes of metal NPs.[28,34,35,44−60]

In this study, we investigated the formation process of anisotropic platinum NPs by in situ SAXS experiments to gain insight into the optimization of the process parameters. Real-time measurements monitor continuous changes in the shape of the platinum NPs during the reactions. The randomly distributed rod model (Figure 1a) was applied to elucidate the shape, size, number density, reaction yield, and SSA of the platinum NPs. Monitoring during three different heating sequences (see Figure 2a) enabled us to discuss the growth mechanism of anisotropic platinum NPs and propose process parameters aimed at shape control for fuel cell applications.

■ RESULTS AND DISCUSSION

Figure S1 shows the TEM images of platinum NPs synthesized by heating at sequence **3** (T_R = 100 °C, t_R = 75 min). In this study, small amounts of nickel acetylacetonate and molybdenum hexacarbonyl were added to inhibit particle enlargement and prevent particle aggregation[14] (see the Experimental Section). Energy-dispersive X-ray spectroscopy analysis confirmed that the particles were formed from pure platinum (>98%) (Figure S1). The 2D SAXS pattern of platinum NPs synthesized by heating at sequence **1** (T_R = 160 °C, t_R = 100 min) shows an isotropic pattern (Figure 1b), indicating the absence of orientated platinum NPs dispersed in oleylamine. If the particle shape is unclear, then distance distribution function (DDF) analysis would be a powerful tool because neither approximation nor assumption is employed in the analysis.

Hatakeyama et al.[59] and Morita et al.[60] successfully discussed the growth progress of gold nanorods based on DDF analysis. In the present study, rod-like particles were observed in the TEM images sampled under different reaction conditions (Figure S2). Therefore, the randomly distributed rod model (Figure 1a) was applied to elucidate the shape, size, number density, reaction yield, and SSA of the platinum NPs. Although particles after reactions (Figure S3) can be fitted with both sphere and rod models, we employed the rod model overall reactions to systematically investigate time-sliced parameter changes among sequences. Additionally, we noted that the isotropic 2D SAXS patterns (Figure 1b) support the assumption of a randomly distributed rod model. The circular-averaged absolute scattering intensities were plotted as a function of the q-scale (Figure 1c). These profiles have a crossover q^{-1}-dependence to q^{-4}-dependence at $q \sim 0.1$ Å^{-1}. The q^{-1}-dependence is a typical feature of the rod shape, and the crossover point corresponds to the rod radius. Moreover, the scattering intensities point upward at $q < 0.2$ Å^{-1}, which can be well explained by the model of randomly distributed rods (shown as a solid line). Detailed analytical results are discussed later.

Figure 2a shows three heating sequences for the synthesis of platinum NPs in time-resolved SAXS experiments. The scattering data after each heating sequence is shown in Figure

https://doi.org/10.1021/acsomega.1c00608
ACS Omega 2021, 6, 10866−10874

S4. These profiles have the typical features of randomly distributed rods, as mentioned above. It is worth noting that the Debye−Scherrer ring (indicated by the black arrow) was observed after sequence **3** (Figure S4c), suggesting the presence of a self-assembled structure of platinum NPs. The self-assembled structure during the reaction has attracted significant interest because it is believed to be related to particle growth.[44,55] Figure 2b−d shows waterfall plots of time-resolved SAXS profiles obtained using each heating protocol (sequences **1**−**3**). A plateau was observed in the first scan, indicating the absence of platinum NPs before the heating treatment. The most characteristic change is a monotonic increase in the scattering intensity at $q < 0.2$ Å^{-1}. This increase in the scattering intensity supports the nucleation and growth of platinum NPs with an increase in the reaction temperature T_R. A continuous upturn in intensity (Figure 2b) was observed as T_R increased at a constant heating rate, whereas a stepwise T_R increase in sequence **3** induced a discontinuous upturn (Figure 2d). When T_R increased abruptly (Figure 2c), platinum NPs formed in a matter of minutes. Sharp peaks originating from the self-assembled structure, as previously discussed, appear and disappear at 0.1 Å^{-1} < q < 0.2 Å^{-1} during reactions. Similar results have been found in the growth process of gold NPs.[44,55,56] However, a discussion of the self-assembled structure is beyond the scope of this work focused on the shape of the platinum NPs.

Figure 3 shows the results of plotting the time-resolved SAXS profiles for each heating sequence against reaction time t_R. All fitting curves were in good agreement with the time-resolved SAXS profiles (Figure S5). Immediately after the start of the reaction, the obtained fitting parameters are scattered. This is because the background at high q regions affects the fitting parameters in the case of weak signals at low q regions. When small particles (rod radius and length < 10 Å) are born immediately after the start of measurement, the spectrum is not beyond the background level. Therefore, information about the small particles is lost in Figure 3. The heating protocol had a pronounced effect on the formation of platinum NPs (Figure 3a,b). The results of sequences **1** and **2** illustrate that the rod radius R [Å] becomes larger as the heating rate decreases (Figure 3a).

In the present study, the rod length L [Å] was not affected by the heating rate (Figure 3b). In sequence **3**, the rods become thicker and shorter as the T_R increases from 100 to 160 °C (Figure 3a,b). The reduction of rod length and aspect ratio in sequence **3** is due to the fragmentation of long rod-shaped particles (see Figure S6). The aspect ratio (=$L/2R$) plotted in Figure 3c demonstrates that anisotropic platinum NPs can be synthesized at a lower reaction temperature and a shorter reaction time. In the present study, all heating sequences ended at T_R = 160 °C, resulting in platinum NPs with a low aspect ratio (∼1.3). The final shape of the platinum NPs estimated from the analysis was matched with the TEM images (see Figure S3). Figure 3d shows the number density of the platinum NPs. In sequences **1** and **2**, the number density increased after the start of the reaction and then remained almost constant. Meanwhile, in sequence **3**, the number density increases as T_R increases from 100 to 160 °C. The rise in N may be due to two processes: (i) the additional nucleation from platinum precursors and (ii) the fragmentation of long rod-shaped particles. The yield of platinum reduction Y [%] ($Y = 100 \times \phi_{Pt(0)}/\phi^0_{Pt(II)}$, where $\phi_{Pt(0)}$ and $\phi^0_{Pt(II)}$ are the volume fractions of the reduced and platinum precursors, respectively) was calculated from $\phi_{Pt(0)}$, which was obtained by multiplying the particle volume V [cm^3] (calculated from the data shown in Figure 3a,b) by the number density of particles N (particles cm^{-3}) (Figure 3d). The value of $\phi^0_{Pt(II)}$ was 0.004167 based on the sample composition. At the end of each sequence, Y was 20−30% (Figure 4a). These values were roughly consistent with those

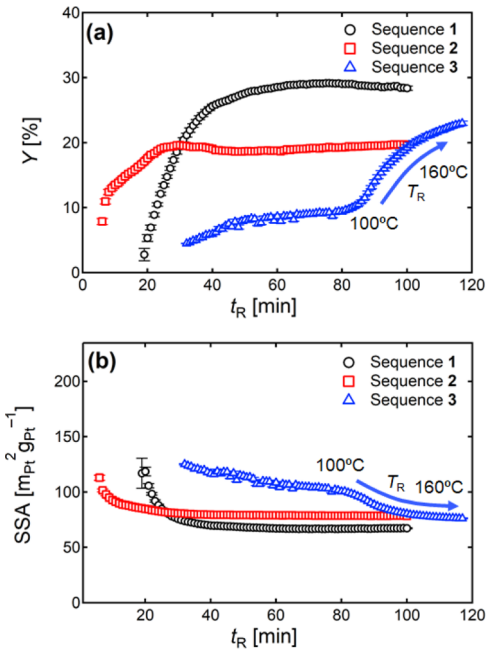

Figure 4. (a) Yield of platinum reduction Y [%] and (b) SSA [m_{Pt}^2 g_{Pt}^{-1}] of platinum NPs as a plot of reaction time t_R [min]. These values were calculated from the obtained fitting parameter displayed in Figure 3.

estimated from the particle weights gathered by centrifuging, washing, and drying in the laboratory. As seen in Figure 4a, a comparison of sequences **1** and **2** supports the fact that the sudden increase in T_R results in a decrease in Y. This is probably because nuclear growth cannot keep up with reductant consumption. In sequence **3**, Y drastically increased at T_R ranging from 100 to 160 °C, which was attributed to an increase in the volume (Figure 3a,b) and the number density of particles (Figure 3d), that is, nuclear growth and nucleation. The simultaneous processes had an impact on particle size distribution (Figure S3c).

We now discuss the optimization of the reaction conditions from in situ time-resolved SAXS experiments. What is the optimal reaction temperature? When should the reaction end? A reasonable answer can be proposed from an electrochemical perspective. Figure 4b displays the dependence of t_R on the SSA, defined as $S_m/(V_m D_{Pt})$, where S_m [m^2], V_m [m^3], and D_{Pt} [g m^{-3}] are the surface area and volume of platinum NPs and the density of platinum (2.145 × 10^7 g m^{-3}), respectively. The Paul Scherrer Institute research group[61] investigated the analogy between ECSA [m_{Pt}^2 g_{Pt}^{-1}] and SSA estimated from anomalous SAXS studies. They reported that the SSA of the catalyst layer consisting of platinum-supported carbon catalysts (TEC10V30E) and the ionomer (Nafion 117 dispersion) with an ECSA of 65 was 107 m_{Pt}^2 g_{Pt}^{-1}. An ECSA value lower than that of the SSA was explained by the aggregation of catalyst NPs.[61] Therefore, although a high SSA does not necessarily

https://doi.org/10.1021/acsomega.1c00608
ACS Omega 2021, 6, 10866−10874

indicate a high ECSA, SSA is an indicator of a desirable particle shape for fuel cell applications. In the present study, the largest SSA (>120 m_{Pt}^2 g_{Pt}^{-1}) was observed in sequence **3** (Figure 4b). Holding at T_R = 100 °C and a shorter reaction time (∼30 min) is suitable for acquiring anisotropic platinum NPs with a higher SSA. However, *Y* decreased from 30 to 10% when the reaction was stopped at a shorter reaction time (Figure 4a). This problem persists in fuel cell applications.

Let us now discuss the growth mechanism and its parameters for shape control. Complex formation is promoted by the action of the polar head of cetyltrimethylammonium chloride (CTAC), which adsorbs onto the platinum surface and is stabilized by the hydrocarbon chain of CTAC located on the oleylamine side.[26] Previous reports have demonstrated that the amounts of CTAC, metal acetylacetonate, and metal carbonyl all affect the particle aspect ratio.[14] In the absence or insufficiency of these agents, spherical NPs and their aggregates are formed. In this work, we discuss the growth mechanism with a focus on the surfactant geometry and T_R. The growth mechanism inferred from the in situ time-resolved SAXS experiments is illustrated in Figure 5. The affinity between the platinum surface and the hydrophilic head of the surfactant depends on the curvature of the platinum surface. Surfactants are likely to be adsorbed on the longitudinal site rather than the end-cap site;[62−64] it is only possible to validate this interfacial structure by contrast-variation small-angle neutron scattering.[65−69] Therefore, the precursor is reduced on the end-cap side (there is no "attack" on the longitudinal site). The possibility of the growth originating from the connection of small particles has been eliminated from the result of high-resolution TEM observations (see Figure S6). This is consistent with those of previous studies.[14] The frequency of nuclear growth increases on the bare end-cap site at a moderate reaction temperature, T_{R1} (illustrated in Figure 5). However, Figure 3b shows an obvious drop in the rod length and aspect ratio in the first 40 min in sequence **3** (see also Figure S2). This trend suggests that even under moderate reaction conditions, nuclear growth on the longitudinal site cannot be ignored when the reaction time is increased.

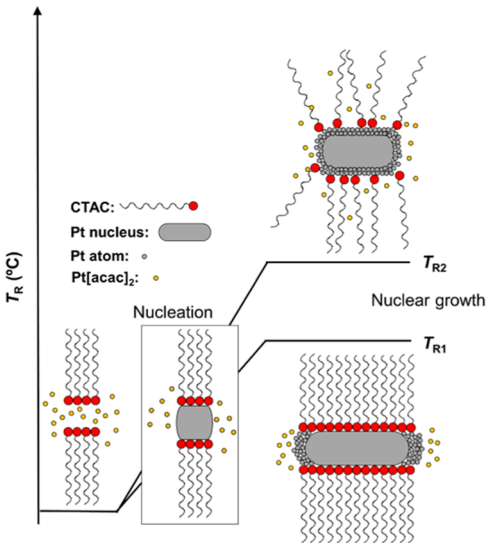

Figure 5. Possible growth mechanism for anisotropic platinum NPs. CTAC forms cylindrical micelles. After spherical particles are generated at nucleation, they form anisotropic NPs via nuclear growth. Arrangement of CTAC on the longitudinal site of the Pt nucleus assists anisotropic growth as more platinum precursors Pt[acac]$_2$ (yellow dots) are introduced to the nucleus as platinum atoms (gray dots) at moderate reaction temperature T_{R1}. At high reaction temperature T_{R2}, platinum precursors easily attack the longitudinal site resulting in isotropic nuclear growth.

It is well known that CTAC forms cylindrical micelles above its critical micelle concentration.[17] In this work, CTAC was added well above the critical micelle concentration (see the Experimental Section). The micelle structure of surfactants is directly related to the particle shape in the seed-mediated colloid growth method.[63] The persistence length of micelles depends strongly on the scission energy: the surface charge and end-cap energy of the micelles.[70] Kusano et al.[71] found that the end-cap energy was strongly related to the surfactant geometry. More intuitively, the ease of end capping can be explained using the surfactant packing parameter proposed by Israelachvili et al.[72] The unitless packing parameter *p* is defined as $p = v/Al$, where v [cm^3] is the effective volume of the hydrocarbon chain, A [cm^2] is the effective area of the polar headgroup, and l [cm] is the length of the hydrocarbon chain. Because the polar head of the surfactant is adsorbed onto the platinum surface in this system, a surfactant with $p > 1$ that forms an inverted micelle structure easily adsorbs onto the end cap and suppresses nuclear growth at this site. However, a surfactant with $p < 1$ destabilizes the adsorption state at the end-cap site, which leads to the growth of anisotropic NPs. The packing parameter of CTAC was lower than 1, indicating that CTAC stabilized the exposed end-cap state. A surfactant with a longer hydrophobic chain instead of CTAC, for example, octadecyltrimethylammonium chloride, would be preferable for enhancing the aspect ratio of platinum NPs. Huang et al. reported the synthesis of platinum-based shape-control catalysts using the surfactant geometry.[73] However, a systematic study focusing on the packing parameter has not yet been performed. For the synthesis of shape-controlled gold NPs in an aqueous medium, the packing parameter was strategically coordinated by the hydrocarbon length of surfactants,[63] pH,[74,75] and electrostatic shielding.[76] Shape-controlled platinum NPs can be designed by controlling the surfactant geometry; however, pH adjustment and salt addition are not effective in lipophilic oleylamine.

In the following, we discuss the influence of the heating rate and T_R on the aspect ratio of platinum NPs. Surfactants do not have a fixed structure; their micelle structure is constantly formed and disrupted in dynamic equilibrium; therefore, rapid heating is not recommended. Although the number density of particles was almost constant in sequences **1** and **3**, the number density of particles decreased within 40 min in sequence **2** (Figure 3d). The reduction could be explained by the presence of a coalescence process due to the inability of the protection provided by surfactants to keep up with rapid heating. The Gibbs energy ($\Delta G = \Delta H - T\Delta S$) determines whether the surfactant promotes the formation of micelles. In general, the entropy term $T\Delta S$ is dominant in micelle formation, so the "soft template" is likely to collapse at a high reaction temperature T_{R2} (illustrated in Figure 5). Platinum precursors easily attack the longitudinal site at T_{R2}, resulting in isotropic nuclear growth. This hypothesis was supported by a study by Gou and Murphy.[77] Their paper reported that additional input of ascorbic acid as a reductant preferentially deposits more metal at the end-cap site, and heat treatment induces deposition on the entire particle surface. In the case of

https://doi.org/10.1021/acsomega.1c00608
ACS Omega 2021, 6, 10866−10874

platinum, previous studies proposed the use of glucose as a reductant, but this requires a high reaction temperature (>100 °C).[14]

CONCLUSIONS

We investigated the formation process of anisotropic platinum NPs synthesized by the reduction of a platinum complex in the presence of a soft template formed by CTAC in oleylamine using in situ SAXS. Time-resolved measurements displayed scattering data that supported the nucleation and growth of platinum NPs during the reactions. Furthermore, time-resolved scans captured diverse shapes every 60 s during the reaction. We successfully established a fitting model to elucidate the shape, size, number density, reaction yield, and SSA of the platinum NPs in each scan. The growth mechanism of platinum NPs is reasonably explained by the distinct local packing motifs of the surfactants and their stability. It was found that platinum NPs with high aspect ratios appeared at lower reaction temperatures (∼100 °C) and shorter reaction times (∼30 min); however, the reaction yield decreased from 30 to 10% when the reaction was stopped under these conditions. A novel synthesis protocol at lower reaction temperatures would lead to the development of favorable platinum catalysts for fuel cell applications.

EXPERIMENTAL SECTION

Sample Preparation for In Situ Time-Resolved SAXS Measurements. Platinum acetylacetonate $Pt(acac)_2$ (10 mg) and CTAC (32 mg) were dissolved in oleylamine (5 mL). In this sample specification, the CTAC concentration was well above its critical micelle concentration. In addition, nickel acetylacetonate $Ni(acac)_2$ (6.4 mg) and molybdenum hexacarbonyl $Mo(CO)_6$ (3 mg) were added to inhibit particle enlargement and prevent particle aggregation, respectively.[14] The mixture was ultrasonicated for 1 h and then heated using three different heating sequences, **1**−**3**, as shown in Figure 2a.

In Situ Time-Resolved SAXS Measurements and Data Conversion. In situ time-resolved SAXS experiments were performed at BL8S3 at the Aichi Synchrotron Radiation Center (Aichi-SR). The ultrasonicated mixture was placed into three Kapton tubes with a diameter of 2 mm. The tubes were annealed during each heating sequence (sequences **1**−**3**) on a hot stage (LK-600PM, Linkam Scientific Instruments Ltd.). The SAXS data were recorded with an X-ray wavelength of 0.92 Å using a 2D pixel detector (PILATUS 100 K, DECTRIS Ltd.). The exposure time for each data set was set to 58 s because the total interval of each measurement was 60 s. The sample-to-detector distance was fixed at 1.16 m. This setup covers momentum transfers ($q \equiv 4\pi \sin \theta/\lambda$, where 2θ [rad] and λ [Å] are the scattering angle and the wavelength of the X-ray, respectively) ranging from 0.04 to 0.4 $Å^{-1}$. Scattering from empty cells was subtracted from all SAXS data. After circular averaging, 1D scattering data were converted from relative to absolute intensity using a pre-calibrated glassy carbon reference provided by the National Institute of Standards and Technology.[78]

Fitting Model and Data Analysis for SAXS Data. In this system, the absolute scattering intensity $I_{abs}(q)$ [cm^{-1}] can be expressed as

$$I_{abs}(q) = (\rho_{Pt} - \rho_{OAm})^2 NV^2 P(q)S(q) + I_{bkg}(q) \quad (1)$$

where ρ_{Pt} [cm^{-2}] and ρ_{OAm} [cm^{-2}] are the scattering length densities of platinum and oleylamine, respectively. N [particles cm^{-3}] and V [cm^3] are the number density and volume of the platinum NPs, respectively. The unitless $P(q)$ and $S(q)$ are the form and structure factors of platinum NPs, respectively, and $I_{bkg}(q)$ [cm^{-1}] is the background scattering intensity mainly derived from oleylamine. In this work, $P(q)$ was modeled using monodisperse rods, and $S(q)$ was approximated as 1. For a rod with radius R [Å] and length L [Å] oriented in the direction of angle α [rad] for the referential axis, the scattering amplitude $A_{rod}(q)$ is given by

$$A_{rod}(q) = \frac{2J_1(qR \sin \alpha)}{qR \sin \alpha} \frac{\sin(q(L/2)\cos \alpha)}{q(L/2)\cos \alpha} \quad (2)$$

where $J_1(x)$ is the Bessel function of the order 1. The form factor of a rod is expressed as

$$P_{rod}(q) = |A_{rod}(q)|^2 \quad (3)$$

Given that rods are randomly distributed in oleylamine, the above form factor should be corrected for orientational averaging as follows

$$P_{rod}^{ave}(q) = \int_0^{\pi/2} P_{rod}(q;\ \alpha)\sin \alpha\ d\alpha / \int_0^{\pi/2} \sin \alpha\ d\alpha \quad (4)$$

ASSOCIATED CONTENT

Supporting Information

The Supporting Information is available free of charge at https://pubs.acs.org/doi/10.1021/acsomega.1c00608.

Energy-dispersive X-ray spectroscopy analysis of synthesized platinum NPs, TEM images of synthesized platinum NPs sampled at different reaction conditions, TEM images of synthesized platinum NPs at each time-resolved SAXS measurement, 2D and 1D SAXS patterns for synthesized platinum NPs, and all fitting curves for each time-resolved SAXS scan (PDF)

AUTHOR INFORMATION

Corresponding Authors

Wataru Yoshimune − *Toyota Central R&D Labs, Inc., Nagakute, Aichi 480-1192, Japan*; orcid.org/0000-0001-8768-0122; Email: e1707@mosk.tytlabs.co.jp

Akira Kuwaki − *Toyota Central R&D Labs, Inc., Nagakute, Aichi 480-1192, Japan*; Email: a-kuwaki@mosk.tytlabs.co.jp

Authors

Takumi Kusano − *Toyota Central R&D Labs, Inc., Nagakute, Aichi 480-1192, Japan*; orcid.org/0000-0002-1114-585X

Takuro Matsunaga − *Toyota Central R&D Labs, Inc., Nagakute, Aichi 480-1192, Japan*

Hiroshi Nakamura − *Toyota Central R&D Labs, Inc., Nagakute, Aichi 480-1192, Japan*

Complete contact information is available at: https://pubs.acs.org/10.1021/acsomega.1c00608

Author Contributions

W.Y. proposed the research, carried out SAXS experiments and data analysis, and wrote the manuscript. A.K. prepared the samples and performed the TEM observations. T.K. and T.M.

https://doi.org/10.1021/acsomega.1c00608
ACS Omega 2021, 6, 10866−10874

conducted the SAXS experiments. H.N. reviewed and revised the manuscript. All authors discussed the results and contributed to the review of the manuscript. All authors approved the final version of the manuscript.

Notes

The authors declare no competing financial interest.

■ ACKNOWLEDGMENTS

The SAXS experiments were performed at the BL8S3 of the Aichi Synchrotron Radiation Center, Aichi Science and Technology Foundation, Aichi, Japan (proposal nos. 2020P3106 and 2020P4106).

■ REFERENCES

(1) Hutter, E.; Fendler, J. H. Exploitation of Localized Surface Plasmon Resonance. *Adv. Mater.* **2004**, *16*, 1685−1706.

(2) Willets, K. A.; Van Duyne, R. P. Localized Surface Plasmon Resonance Spectroscopy and Sensing. *Annu. Rev. Phys. Chem.* **2007**, *58*, 267−297.

(3) Hori, H.; Teranishi, T.; Nakae, Y.; Seino, Y.; Miyake, M.; Yamada, S. Anomalous Magnetic Polarization Effect of Pd and Au Nano-Particles. *Phys. Lett. A* **1999**, *263*, 406−410.

(4) Yamamoto, Y.; Miura, T.; Suzuki, M.; Kawamura, N.; Miyagawa, H.; Nakamura, T.; Kobayashi, K.; Teranishi, T.; Hori, H. Direct Observation of Ferromagnetic Spin Polarization in Gold Nanoparticles. *Phys. Rev. Lett.* **2004**, *93*, 116801.

(5) Haruta, M.; Kobayashi, T.; Sano, H.; Yamada, N. Novel Gold Catalysts for the Oxidation of Carbon Monoxide at a Temperature Far Below 0 °C. *Chem. Lett.* **1987**, *16*, 405−408.

(6) Corma, A.; Serna, P. Chemoselective Hydrogenation of Nitro Compounds with Supported Gold Catalysts. *Science* **2006**, *313*, 332−334.

(7) Bakshi, M. S. How Surfactants Control Crystal Growth of Nanomaterials. *Cryst. Growth Des.* **2016**, *16*, 1104−1133.

(8) Kongkanand, A.; Mathias, M. F. The Priority and Challenge of High-Power Performance of Low-Platinum Proton-Exchange Membrane Fuel Cells. *J. Phys. Chem. Lett.* **2016**, *7*, 1127−1137.

(9) Pan, L.; Ott, S.; Dionigi, F.; Strasser, P. Current Challenges Related to the Deployment of Shape-Controlled Pt Alloy Oxygen Reduction Reaction Nanocatalysts into Low Pt-Loaded Cathode Layers of Proton Exchange Membrane Fuel Cells. *Curr. Opin. Electrochem.* **2019**, *18*, 61−71.

(10) Liu, M.; Zhao, Z.; Duan, X.; Huang, Y. Nanoscale Structure Design for High-Performance Pt-Based ORR Catalysts. *Adv. Mater.* **2019**, *31*, 1802234.

(11) Cui, C.; Gan, L.; Heggen, M.; Rudi, S.; Strasser, P. Compositional Segregation in Shaped Pt Alloy Nanoparticles and Their Structural Behaviour During Electrocatalysis. *Nat. Mater.* **2013**, *12*, 765−771.

(12) Chen, C.; Kang, Y.; Huo, Z.; Zhu, Z.; Huang, W.; Xin, H. L.; Snyder, J. D.; Li, D.; Herron, J. A.; Mavrikakis, M.; Chi, M.; More, K. L.; Li, Y.; Markovic, N. M.; Somorjai, G. A.; Yang, P.; Stamenkovic, V. R. Highly Crystalline Multimetallic Nanoframes with Three-Dimensional Electrocatalytic Surfaces. *Science* **2014**, *343*, 1339−1343.

(13) Bu, L.; Zhang, N.; Guo, S.; Zhang, X.; Li, J.; Yao, J.; Wu, T.; Lu, G.; Ma, J.-Y.; Su, D.; Huang, X. Biaxially Strained PtPb/Pt Core/Shell Nanoplate Boosts Oxygen Reduction Catalysis. *Science* **2016**, *354*, 1410−1414.

(14) Jiang, K.; Zhao, D.; Guo, S.; Zhang, X.; Zhu, X.; Guo, J.; Lu, G.; Huang, X. Efficient Oxygen Reduction Catalysis by Subnanometer Pt Alloy Nanowires. *Sci. Adv.* **2017**, *3*, No. e1601705.

(15) Li, M.; Zhao, Z.; Cheng, T.; Fortunelli, A.; Chen, C.-Y.; Yu, R.; Zhang, Q.; Gu, L.; Merinov, B. V.; Lin, Z.; Zhu, E.; Yu, T.; Jia, Q.; Guo, J.; Zhang, L.; Goddard, W. A.; Huang, Y.; Duan, X., III; Huang, Y.; Duan, X. Ultrafine Jagged Platinum Nanowires Enable Ultrahigh Mass Activity for the Oxygen Reduction Reaction. *Science* **2016**, *354*, 1414−1419.

(16) Sievers, G. W.; Jensen, A. W.; Quinson, J.; Zana, A.; Bizzotto, F.; Oezaslan, M.; Dworzak, A.; Kirkensgaard, J. J. K.; Smitshuysen, T. E. L.; Kadkhodazadeh, S.; Juelsholt, M.; Jensen, K. M. Ø.; Anklam, K.; Wan, H.; Schäfer, J.; Čépe, K.; Escudero-Escribano, M.; Rossmeisl, J.; Quade, A.; Brüser, V.; Arenz, M. Self-Supported Pt−CoO Networks Combining High Specific Activity with High Surface Area for Oxygen Reduction. *Nat. Mater.* **2021**, *20*, 208−213.

(17) Lohse, S. E.; Murphy, C. J. The Quest for Shape Control: A History of Gold Nanorod Synthesis. *Chem. Mater.* **2013**, *25*, 1250−1261.

(18) Jain, P. K.; Huang, X.; El-Sayed, I. H.; El-Sayed, M. A. Noble Metals on the Nanoscale: Optical and Photothermal Properties and Some Applications in Imaging, Sensing, Biology, and Medicine. *Acc. Chem. Res.* **2008**, *41*, 1578−1586.

(19) Tian, M.; Wang, J.; Kurtz, J.; Mallouk, T. E.; Chan, M. H. W. Electrochemical Growth of Single-Crystal Metal Nanowires via a Two-Dimensional Nucleation and Growth Mechanism. *Nano Lett.* **2003**, *3*, 919−923.

(20) Kim, F.; Song, J. H.; Yang, P. Photochemical Synthesis of Gold Nanorods. *J. Am. Chem. Soc.* **2002**, *124*, 14316−14317.

(21) Murphy, C. J.; Thompson, L. B.; Chernak, D. J.; Yang, J. A.; Sivapalan, S. T.; Boulos, S. P.; Huang, J.; Alkilany, A. M.; Sisco, P. N. Gold Nanorod Crystal Growth: From Seed-Mediated Synthesis to Nanoscale Sculpting. *Curr. Opin. Colloid Interface Sci.* **2011**, *16*, 128−134.

(22) Quinson, J.; Jensen, K. M. Ø. From Platinum Atoms in Molecules to Colloidal Nanoparticles: A Review on Reduction, Nucleation and Growth Mechanisms. *Adv. Colloid Interface Sci.* **2020**, *286*, 102300.

(23) Cheong, S.; Watt, J. D.; Tilley, R. D. Shape Control of Platinum and Palladium Nanoparticles for Catalysis. *Nanoscale* **2010**, *2*, 2045−2053.

(24) Quinson, J.; Inaba, M.; Neumann, S.; Swane, A. A.; Bucher, J.; Simonsen, S. B.; Theil Kuhn, L.; Kirkensgaard, J. J. K.; Jensen, K. M. Ø.; Oezaslan, M.; Kunz, S.; Arenz, M. Investigating Particle Size Effects in Catalysis by Applying a Size-Controlled and Surfactant-Free Synthesis of Colloidal Nanoparticles in Alkaline Ethylene Glycol: Case Study of the Oxygen Reduction Reaction on Pt. *ACS Catal.* **2018**, *8*, 6627−6635.

(25) Cargnello, M.; Chen, C.; Diroll, B. T.; Doan-Nguyen, V. V. T.; Gorte, R. J.; Murray, C. B. Efficient Removal of Organic Ligands from Supported Nanocrystals by Fast Thermal Annealing Enables Catalytic Studies on Well-Defined Active Phases. *J. Am. Chem. Soc.* **2015**, *137*, 6906−6911.

(26) Fan, X.; Luo, S.; Zhao, X.; Wu, X.; Luo, Z.; Tang, M.; Chen, W.; Song, X.; Quan, Z. One-Nanometer-Thick Platinum-Based Nanowires with Controllable Surface Structures. *Nano Res.* **2019**, *12*, 1721−1726.

(27) Song, Y.; Garcia, R. M.; Dorin, R. M.; Wang, H.; Qiu, Y.; Coker, E. N.; Steen, W. A.; Miller, J. E.; Shelnutt, J. A. Synthesis of Platinum Nanowire Networks Using a Soft Template. *Nano Lett.* **2007**, *7*, 3650−3655.

(28) Polte, J.; Tuaev, X.; Wuithschick, M.; Fischer, A.; Thuenemann, A. F.; Rademann, K.; Kraehnert, R.; Emmerling, F. Formation Mechanism of Colloidal Silver Nanoparticles: Analogies and Differences to the Growth of Gold Nanoparticles. *ACS Nano* **2012**, *6*, 5791−5802.

(29) Wang, Y.; Ren, J.; Deng, K.; Gui, L.; Tang, Y. Preparation of Tractable Platinum, Rhodium, and Ruthenium Nanoclusters with Small Particle Size in Organic Media. *Chem. Mater.* **2000**, *12*, 1622−1627.

(30) Herricks, T.; Chen, J.; Xia, Y. Polyol Synthesis of Platinum Nanoparticles: Control of Morphology with Sodium Nitrate. *Nano Lett.* **2004**, *4*, 2367−2371.

(31) Steinfeldt, N. In Situ Monitoring of Pt Nanoparticle Formation in Ethylene Glycol Solution by SAXS Influence of the NaOH to Pt Ratio. *Langmuir* **2012**, *28*, 13072−13079.

(32) Saha, D.; Bøjesen, E. D.; Jensen, K. M. Ø.; Dippel, A.-C.; Iversen, B. B. Formation Mechanisms of Pt and Pt_3Gd Nanoparticles

under Solvothermal Conditions: An In Situ Total X-ray Scattering Study. *J. Phys. Chem. C* **2015**, *119*, 13357−13362.
(33) El-Sayed, H. A.; Burger, V. M.; Miller, M.; Wagenbauer, K.; Wagenhofer, M.; Gasteiger, H. A. Ionic Conductivity Measurements-A Powerful Tool for Monitoring Polyol Reduction Reactions. *Langmuir* **2017**, *33*, 13615−13624.
(34) Quinson, J.; Mathiesen, J. K.; Schröder, J.; Dworzak, A.; Bizzotto, F.; Zana, A.; Simonsen, S. B.; Theil Kuhn, L.; Oezaslan, M.; Jensen, K. M. Ø.; Arenz, M. Teaching Old Precursors New Tricks: Fast Room Temperature Synthesis of Surfactant-Free Colloidal Platinum Nanoparticles. *J. Colloid Interface Sci.* **2020**, *577*, 319−328.
(35) Quinson, J.; Dworzak, A.; Simonsen, S. B.; Theil Kuhn, L.; Jensen, K. M. Ø.; Zana, A.; Oezaslan, M.; Kirkensgaard, J. J. K.; Arenz, M. Surfactant-Free Synthesis of Size Controlled Platinum Nanoparticles: Insights From In Situ Studies. *Appl. Surf. Sci.* **2021**, *549*, 149263.
(36) Kimura, Y.; Abe, D.; Ohmori, T.; Mizutani, M.; Harada, M. Synthesis of Platinum Nanoparticles in High-Temperatures and High-Pressures Fluids. *Colloids Surf., A* **2003**, *231*, 131−141.
(37) Harada, M.; Ueji, M.; Kimura, Y. Synthesis of Colloidal Particles of Poly(2-vinylpyridine)-Coated Palladium and Platinum in Organic Solutions under the High Temperatures and High Pressures. *Colloids Surf., A* **2008**, *315*, 304−310.
(38) Liao, H.-G.; Cui, L.; Whitelam, S.; Zheng, H. Real-Time Imaging of Pt_3Fe Nanorod Growth in Solution. *Science* **2012**, *336*, 1011−1014.
(39) Wu, S.; Li, M.; Sun, Y. In Situ Synchrotron X-ay Characterization Shining Light on the Nucleation and Growth Kinetics of Colloidal Nanoparticles. *Angew. Chem., Int. Ed.* **2019**, *58*, 8987−8995.
(40) Yao, T.; Liu, S.; Sun, Z.; Li, Y.; He, S.; Cheng, H.; Xie, Y.; Liu, Q.; Jiang, Y.; Wu, Z.; Pan, Z.; Yan, W.; Wei, S. Probing Nucleation Pathways for Morphological Manipulation of Platinum Nanocrystals. *J. Am. Chem. Soc.* **2012**, *134*, 9410−9416.
(41) Harada, M.; Kamigaito, Y. Nucleation and Aggregative Growth Process of Platinum Nanoparticles Studied by In Situ Quick XAFS Spectroscopy. *Langmuir* **2012**, *28*, 2415−2428.
(42) Harada, M.; Kizaki, S. Formation Mechanism of Gold Nanoparticles Synthesized by Photoreduction in Aqueous Ethanol Solutions of Polymers Using In Situ Quick Scanning X-ray Absorption Fine Structure and Small-Angle X ray Scattering. *Cryst. Growth Des.* **2016**, *16*, 1200−1212.
(43) Abécassis, B.; Testard, F.; Spalla, O.; Barboux, P. Probing In Situ the Nucleation and Growth of Gold Nanoparticles by Small-Angle X-Ray Scattering. *Nano Lett.* **2007**, *7*, 1723−1727.
(44) Abécassis, B.; Testard, F.; Spalla, O. Gold Nanoparticle Superlattice Crystallization Probed *In Situ*. *Phys. Rev. Lett.* **2008**, *100*, 115504.
(45) Abécassis, B.; Testard, F.; Kong, Q.; Francois, B.; Spalla, O. Influence of Monomer Feeding on a Fast Gold Nanoparticles Synthesis: Time-Resolved XANES and SAXS Experiments. *Langmuir* **2010**, *26*, 13847−13854.
(46) Hubert, F.; Testard, F.; Thill, A.; Kong, Q.; Tache, O.; Spalla, O. Growth and Overgrowth of Concentrated Gold Nanorods: Time Resolved SAXS and XANES. *Cryst. Growth Des.* **2012**, *12*, 1548−1555.
(47) Chen, X.; Schröder, J.; Hauschild, S.; Rosenfeldt, S.; Dulle, M.; Förster, S. Simultaneous SAXS/WAXS/UV−Vis Study of the Nucleation and Growth of Nanoparticles: A Test of Classical Nucleation Theory. *Langmuir* **2015**, *31*, 11678−11691.
(48) Chen, X.; Wei, M.; Jiang, S.; Förster, S. Two Growth Mechanisms of Thiol-Capped Gold Nanoparticles Controlled by Ligand Chemistry. *Langmuir* **2019**, *35*, 12130−12138.
(49) Polte, J.; Erler, R.; Thünemann, A. F.; Sokolov, S.; Ahner, T. T.; Rademann, K.; Emmerling, F.; Kraehnert, R. Nucleation and Growth of Gold Nanoparticles Studied via In Situ Small Angle X-Ray Scattering at Millisecond Time Resolution. *ACS Nano* **2010**, *4*, 1076−1082.
(50) Polte, J.; Erler, R.; Thünemann, A. F.; Emmerling, F.; Kraehnert, R. SAXS in Combination with a Free Liquid Jet for Improved Time-Resolved In Situ Studies of the Nucleation and Growth of Nanoparticles. *Chem. Commun.* **2010**, *46*, 9209−9211.
(51) Polte, J.; Emmerling, F.; Radtke, M.; Reinholz, U.; Riesemeier, H.; Thünemann, A. F. Real-Time Monitoring of Copolymer Stabilized Growing Gold Nanoparticles. *Langmuir* **2010**, *26*, 5889−5894.
(52) Polte, J.; Ahner, T. T.; Delissen, F.; Sokolov, S.; Emmerling, F.; Thünemann, A. F.; Kraehnert, R. Mechanism of Gold Nanoparticle Formation in the Classical Citrate Synthesis Method Derived from Coupled In Situ XANES and SAXS Evaluation. *J. Am. Chem. Soc.* **2010**, *132*, 1296−1301.
(53) Plech, A.; Kotaidis, V.; Siems, A.; Sztucki, M. Kinetics of the X-Ray Induced Gold Nanoparticle Synthesis. *Phys. Chem. Chem. Phys.* **2008**, *10*, 3888−3894.
(54) Henkel, A.; Schubert, O.; Plech, A.; Sönnichsen, C. Growth Kinetic of a Rod-Shaped Metal Nanocrystal. *J. Phys. Chem. C* **2009**, *113*, 10390−10394.
(55) Loubat, A.; Impéror-Clerc, M.; Pansu, B.; Meneau, F.; Raquet, B.; Viau, G.; Lacroix, L.-M. Growth and Self-Assembly of Ultrathin Au Nanowires into Expanded Hexagonal Superlattice Studied by In Situ SAXS. *Langmuir* **2014**, *30*, 4005−4012.
(56) Hamon, C.; Constantin, D. Growth Kinetics of Core-Shell Au/Ag Nanoparticles. *J. Phys. Chem. C* **2020**, *124*, 21717−21721.
(57) Koerner, H.; MacCuspie, R. I.; Park, K.; Vaia, R. A. In Situ UV/Vis, SAXS, and TEM Study of Single-Phase Gold Nanoparticle Growth. *Chem. Mater.* **2012**, *24*, 981−995.
(58) Takenaka, Y.; Kitahata, H.; Yamada, N. L.; Seto, H.; Hara, M. Growth of Gold Nanorods in Gelled Surfactant Solutions. *J. Colloid Interface Sci.* **2011**, *356*, 111−117.
(59) Hatakeyama, Y.; Sasaki, K.; Judai, K.; Nishikawa, K.; Hino, K. Growth Behavior of Gold Nanorods Synthesized by the Seed-Mediated Method: Tracking of Reaction Progress by Time-Resolved X-ray Absorption Near-Edge Structure, Small-Angle X-ray Scattering, and Ultraviolet-Visible Spectroscopy. *J. Phys. Chem. C* **2018**, *122*, 7982−7991.
(60) Morita, T.; Tanaka, E.; Inagaki, Y.; Hotta, H.; Shingai, R.; Hatakeyama, Y.; Nishikawa, K.; Murai, H.; Nakano, H.; Hino, K. Aspect-Ratio Dependence on Formation Process of Gold Nanorods Studied by Time-Resolved Distance Distribution Functions. *J. Phys. Chem. C* **2010**, *114*, 3804−3810.
(61) Povia, M.; Herranz, J.; Binninger, T.; Nachtegaal, M.; Diaz, A.; Kohlbrecher, J.; Abbott, D. F.; Kim, B.-J.; Schmidt, T. J. Combining SAXS and XAS to Study the Operando Degradation of Carbon-Supported Pt-Nanoparticle Fuel Cell Catalysts. *ACS Catal.* **2018**, *8*, 7000−7015.
(62) Nikoobakht, B.; El-Sayed, M. A. Evidence for Bilayer Assembly of Cationic Surfactants on the Surface of Gold Nanorods. *Langmuir* **2001**, *17*, 6368−6374.
(63) Gao, J.; Bender, C. M.; Murphy, C. J. Dependence of the Gold Nanorod Aspect Ratio on the Nature of the Directing Surfactant in Aqueous Solution. *Langmuir* **2003**, *19*, 9065−9070.
(64) Sau, T. K.; Murphy, C. J. Self-Assembly Patterns Formed upon Solvent Evaporation of Aqueous Cetyltrimethylammonium Bromide-Coated Gold Nanoparticles of Various Shapes. *Langmuir* **2005**, *21*, 2923−2929.
(65) Shibayama, M.; Matsunaga, T.; Kusano, T.; Amemiya, K.; Kobayashi, N.; Yoshida, T. SANS Studies on Catalyst Ink of Fuel Cell. *J. Appl. Polym. Sci.* **2014**, *131*, 39842.
(66) Balu, R.; Choudhury, N. R.; Mata, J. P.; de Campo, L.; Rehm, C.; Hill, A. J.; Dutta, N. K. Evolution of the Interfacial Structure of a Catalyst Ink with the Quality of the Dispersing Solvent: A Contrast Variation Small-Angle and Ultrasmall-Angle Neutron Scattering Investigation. *ACS Appl. Mater. Interfaces* **2019**, *11*, 9934−9946.
(67) Yoshimune, W.; Harada, M. Effect of Pt Loading on the Adsorption of Perfluoro-Sulfonic Acid Ionomer in Catalyst Ink for Polymer Electrolyte Fuel Cells. *Chem. Lett.* **2019**, *48*, 487−490.
(68) Yoshimune, W.; Harada, M. Impact of Nonadsorbed Ionomer on Viscosity of Catalyst Inks for Polymer Electrolyte Fuel Cells. *Bull. Chem. Soc. Jpn.* **2020**, *93*, 302−307.

(69) Yoshimune, W.; Harada, M.; Akimoto, Y. Small-Angle Neutron Scattering Studies on the Distribution of Polytetrafluoroethylene Within Microporous Layers for Polymer Electrolyte Fuel Cells. *Compos. Part. C: Open Access* **2020**, *2*, 100015.
(70) Jiang, H.; Vogtt, K.; Thomas, J. B.; Beaucage, G.; Mulderig, A. Enthalpy and Entropy of Scission in Wormlike Micelles. *Langmuir* **2018**, *34*, 13956−13964.
(71) Kusano, T.; Iwase, H.; Yoshimura, T.; Shibayama, M. Structural and Rheological Studies on Growth of Salt-Free Wormlike Micelles Formed by Star-Type Trimeric Surfactants. *Langmuir* **2012**, *28*, 16798−16806.
(72) Israelachvili, J. N.; Mitchell, D. J.; Ninham, B. W. Theory of Self-Assembly of Hydrocarbon Amphiphiles into Micelles and Bilayers. *J. Chem. Soc., Faraday Trans. 2* **1976**, *72*, 1525−1568.
(73) Huang, L.; Zhang, X.; Wang, Q.; Han, Y.; Fang, Y.; Dong, S. Shape-Control of Pt-Ru Nanocrystals: Tuning Surface Structure for Enhanced Electrocatalytic Methanol Oxidation. *J. Am. Chem. Soc.* **2018**, *140*, 1142−1147.
(74) Busbee, B. D.; Obare, S. O.; Murphy, C. J. An Improved Synthesis of High-Aspect-Ratio Gold Nanorods. *Adv. Mater.* **2003**, *15*, 414−416.
(75) Kim, F.; Sohn, K.; Wu, J.; Huang, J. Chemical Synthesis of Gold Nanowires in Acidic Solutions. *J. Am. Chem. Soc.* **2008**, *130*, 14442−14443.
(76) Ye, X.; Jin, L.; Caglayan, H.; Chen, J.; Xing, G.; Zheng, C.; Doan-Nguyen, V.; Kang, Y.; Engheta, N.; Kagan, C. R.; Murray, C. B. Improved Size-Tunable Synthesis of Monodisperse Gold Nanorods through the Use of Aromatic Additives. *ACS Nano* **2012**, *6*, 2804−2817.
(77) Gou, L.; Murphy, C. J. Fine-Tuning the Shape of Gold Nanorods. *Chem. Mater.* **2005**, *17*, 3668−3672.
(78) Allen, A. J.; Zhang, F.; Kline, R. J.; Guthrie, W. F.; Ilavsky, J. NIST Standard Reference Material 3600: Absolute Intensity Calibration Standard for Small-Angle X-Ray Scattering. *J. Appl. Crystallogr.* **2017**, *50*, 462−474.

https://doi.org/10.1021/acsomega.1c00608
ACS Omega 2021, 6, 10866−10874